Proc. Indian Acad. Sci. (Earth Planet. Sci.), Vol. 101, No. 2, June 1992, pp. 177–189.

Diurnal and semi-diurnal tidal currents in the deep mid-Arabian Sea

S S C SHENOI, A D GOUVEIA and S R SHETYE
National Institute of Oceanography, Dona Paula, Goa 403 004, India

MS received 21 October 1991; revised 7 March 1992

Abstract. Current meter records from two depths, approximately 1000 and 3000 m, at three moorings in the deep mid-Arabian Sea were used to study tidal components. Tidal ellipses for the semi-diurnal (M_2, S_2 and K_2) and the diurnal (K_1 and P_1) tidal constituents have been determined using the currents recorded at hourly intervals during May 1986–May 1987. The clockwise rotating M_2 tidal currents were the strongest. The maximum horizontal velocities due to M_2, S_2 and K_1 tides were 2·2 cm/s, 1·0 cm/s and 0·89 cm/s respectively. The amplitudes of the other two constituents (P_1 and K_2) were much smaller. The barotropic M_2 ellipses have been estimated by averaging the M_2 tidal currents at the upper and lower levels. Although the amplitudes of computed ellipses are lower than those that have been predicted using numerical models of global tidal model, their orientations are the same.

Keywords. Arabian Sea; tidal currents; diurnal tides; semi-diurnal tides; tidal ellipses.

1. Introduction

The rhythmic rise and fall of the sea level due to the tides, which result from the gravitational pull of the moon and sun, are amongst the more regular and predictable motions in the world oceans. The frequencies of these motions can be defined by a combination of the periodicities observed in the movement of the moon and sun relative to the earth. In general, the tides have periods varying from a few hours to a few years. However, the semi-diurnal ($\simeq$ 12 hours) and diurnal ($\simeq$ 24 hours) periods are the most prominent ones. The tidal undulations of the sea surface associated with these frequencies vary from a few tens of centimeters in the open ocean to a few meters in the coastal waters. To determine and separate these tidal constituents a reasonably long time-series of the oceanic motion is needed. Long-term measurements of vertical movements due to tides, the tidal amplitudes, are generally made with the use of water level recorders installed near the coast, or pressure recorders mounted at the bottom of the deep sea. In recent years the satellite altimeters have also been used to measure tidal elevation (Cartwright and Ray 1990). Unlike tidal elevations, it is difficult to make precise long-term measurements of the currents associated with tides. The difficulties are even more in the deep sea where the tidal currents are weak. Usually, longer time-series are required for tidal current analysis than for tidal height analysis, because signals from other sources generally appear in current meter data.

As the forcing function for tides is known, it is assumed that tidal currents can be calculated by solving tidal equations. Pekeris and Accad (1969), who solved the Laplace tidal equations numerically in a homogeneous world ocean with realistic bottom topography and coastal geometry, provided a global chart of tidal current ellipses due to the principal lunar semi-diurnal (M_2) tide. Schwiderski (1980) carried out

similar numerical experiments to provide the amplitudes and phases of tidal elevations over the world oceans for eleven tidal constituents. In these experiments observed tidal elevations were used to tune the parameters (friction coefficients, for example) used in the numerical model. The tidal charts for M_2, S_2 (solar semi-diurnal), and K_1 (luni-solar diurnal) tidal constituents reproduced from Schwiderski (1979, 1981a, b) are given in figure 1. Schwiderski's tidal charts could achieve an accuracy of 5 cm uniformly over all open oceans. Although the charts of global ocean tides reached a

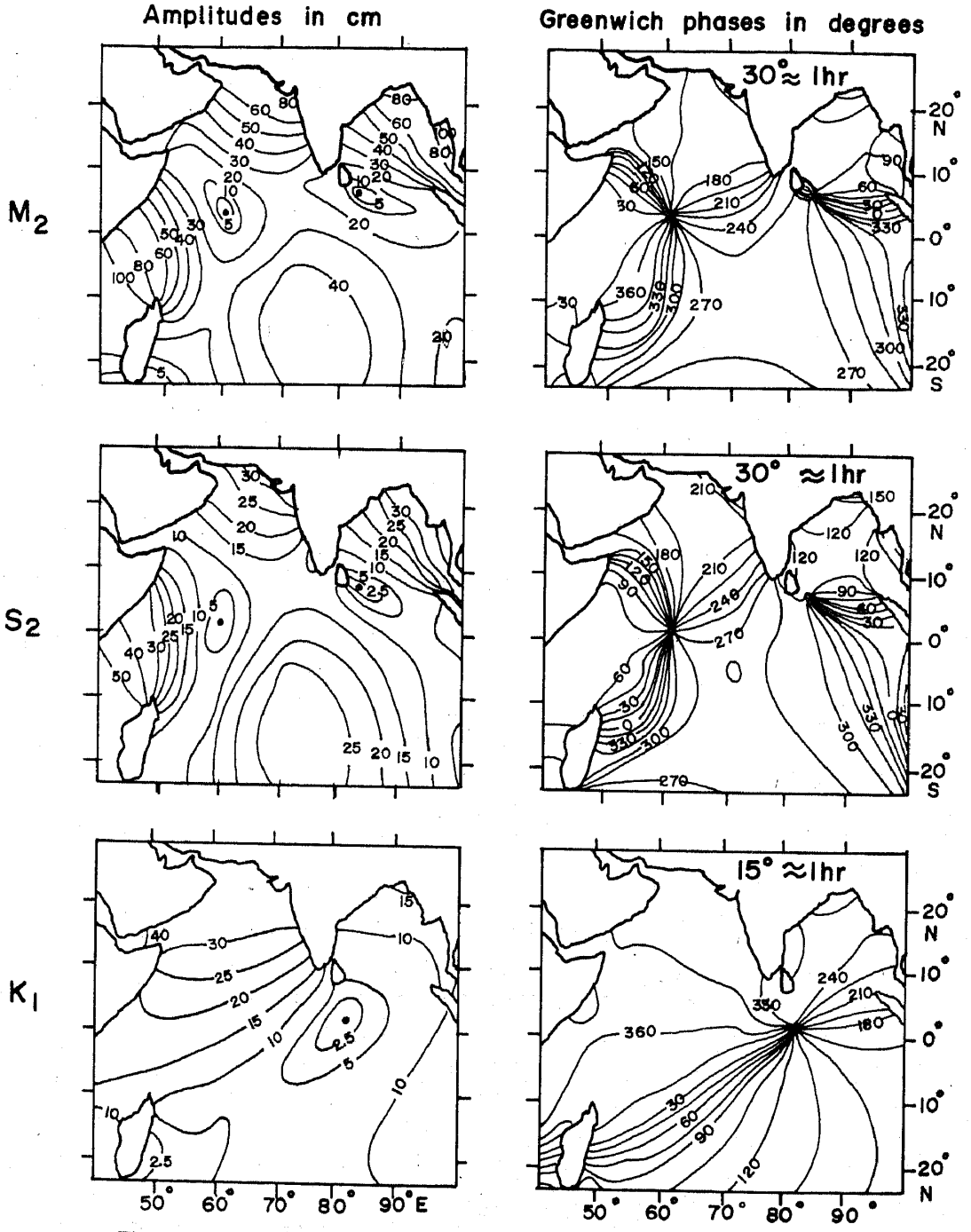

Figure 1. Corange (equal tidal height contours) and cotidal (equal phase contours) charts for M_2, S_2 and K_1 oceanic tides (reproduced from Schwiderski, 1979, 1981a, b).

level of satisfactory accuracy, more and more observations and accurate analysis of long time-series are required to check and improve the established models. The numerical models currently available generally perform better in prediction of sea-level elevation in coastal regions than in the open sea. The main reason for this is that the adjustable parameters in the models are often tuned to match observed elevations in the coastal regions which have most of the world's tide gauges. The models perform better in predicting tidal heights than in predicting tidal currents. The former can be predicted using two-dimensional models which use vertically integrated equations. Tidal currents vary in the vertical and their simulation requires three-dimensional models which are more difficult to formulate and expensive to run. In essence, though the models can make reliable predictions of tidal heights, they are not as useful in predicting tidal currents in the open sea. Direct measurements of currents are therefore necessary to improve our understanding of tidal circulation.

A few earlier studies have described tidal currents from the Atlantic (Gould and McKee 1973; Magaard and Mckee 1973; Regal and Wunsch 1973) and Pacific Oceans (Weisberg *et al* 1987) using long-term direct observations. However, similar studies are not available for the open North Indian ocean. It is with this in view that we took up the analysis of available current records from mid-Arabian Sea.

The M_2, S_2 and K_1 constituents being the dominant ones in the Arabian Sea, we have restricted our discussion mainly to these constituents, though our analysis could separate other constitutents too. The amphidromic points corresponding to M_2 and S_2 tides occur near the equator at about 60°E and southeast of Sri Lanka (figure 1). The only amphidrome corresponding to K_1 lies at 85°E near the equator. The next section describes the data and the method of analysis. Tidal ellipses are derived in §3 and their properties are discussed later.

2. Data analysis

The locations of the three moorings and the major features of bottom topography are shown in figure 2. A general description of the mooring system was given by Shetye *et al* (1991). These measurements were aimed at measuring the advective field in the vicinity of the sediment traps laid to study vertical particle fluxes (Nair *et al* 1989). Two current meters, one at around 1000 m and another at 3000 m from the surface, were hoisted on the moorings. Data at both the levels were recorded every hour by RCM5 Aanderaa Current meters. The shallowest sub-surface buoy, supporting the mooring, was at a depth of about 500 m. The current meters were hoisted in May 1986 serviced in November 1986 and recovered in May 1987. The data records from the central (CAS) mooring ended on 5 November 1986 when both the current meters failed. The bottom current meter at the eastern (EAS) mooring stopped functioning in early September 1986 and the upper meter had a data gap of about 2 months during September–November 1986. The depth of the instruments and the period of data records used in the analysis are indicated in table 1. The tidal analysis reported here is based on the method of least-square fit described by Godin (1972). The algorithms developed by Foreman (1978) were used for this purpose. The observed current vectors were split into u (east-west) and v (north-south) components. Assuming that each of the current component comprises an aperiodic constituent and tidal constituents at frequencies f_j, for $j = 1, 2, \ldots M$, the complex signal, i.e. the current

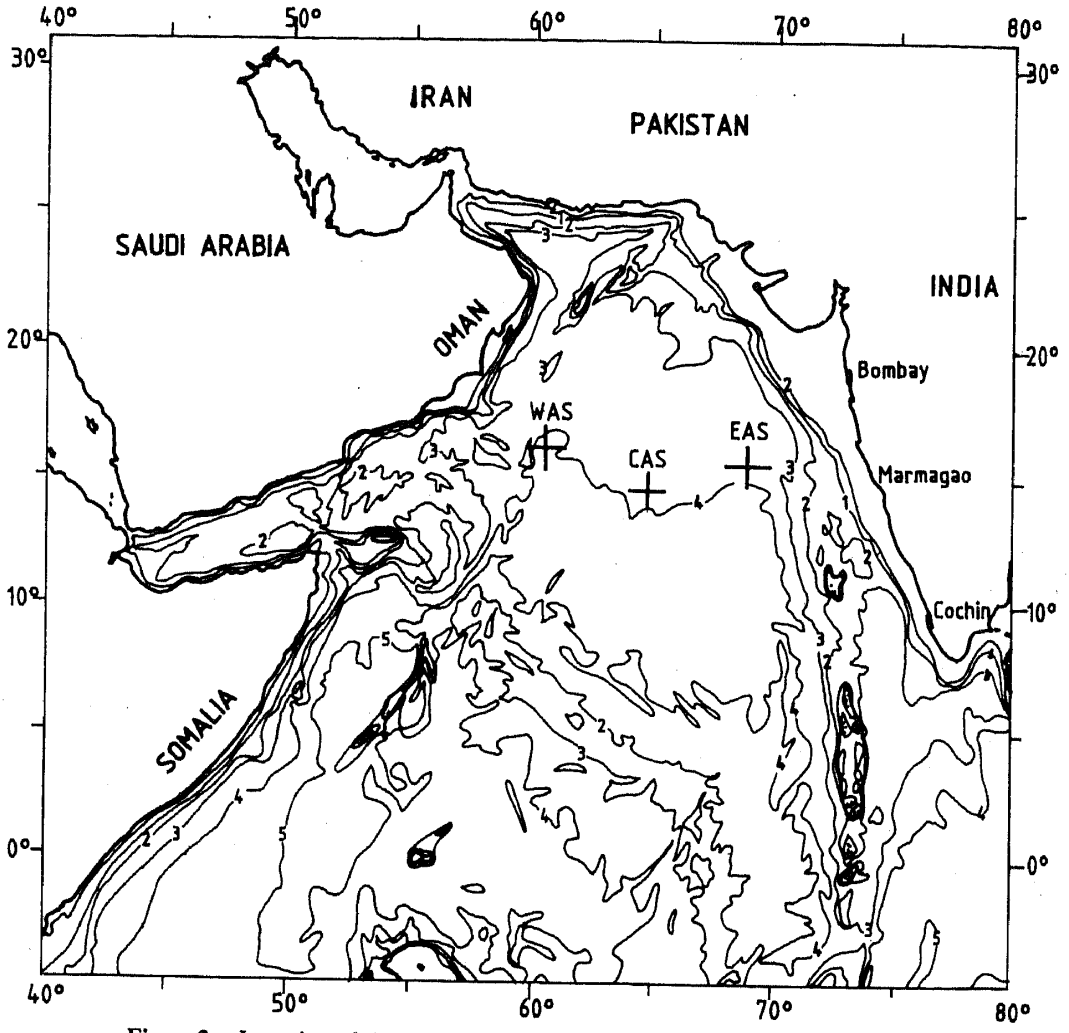

Figure 2. Location of the western (WAS), the central (CAS) and the eastern (EAS) mooring in the Arabian Sea. The depth contours are in km.

Table 1. Mooring locations and the length of records used for the analysis.

	Western mooring (WAS)	Central mooring (CAS)	Eastern mooring (EAS)
Lat	16°23′N	14°31′N	15°32′N
Long	60°32′E	64°42′E	68°44′E
Depth to bottom (*m*)	4016	3906	3779
Depth of upper current meter (*m*)	1016	706	1379
Depth of lower current meter (*m*)	3016	2906	2779
Period of records used from upper meter	4 May 86 to 4 May 87	7 May 86 to 11 Nov 86	9 May 86 to 12 Sep 86
Period of records used from lower meter	6 May 86 to 4 May 87	7 May 86 to 11 Nov 86	10 May 86 to 14 Sep 86

vector, $V(t)$ can be expressed as:

$$V(t) = u_0(t) + \sum_{j=1}^{M} u_j \cos 2\pi(f_j t - \phi_j) + i\left[v_0(t) + \sum_{j=1}^{M} v_j \cos 2\pi(f_j t - \theta_j) \right], \tag{1}$$

where u_j and v_j are the east-west and north-south components of current vector. After expanding the cosines as the sum of cosine and sine terms, the tidal current contribution for any constituent is expressed by (see Foreman 1977 and 1978 for details)

$$V(t) = V^+(t) + V^-(t), \tag{2}$$

$$V(t) = a^+ \exp(i\varepsilon^+ + 2\pi i f t) + a^- \exp(i\varepsilon^- - 2\pi i f t). \tag{3}$$

The above expression shows that the tidal current for each constituent can be written as the sum of two vectors $V^+(t)$ and $V^-(t)$, each rotating at an angular speed of f cycles per hour. The former vector has length a^+, rotates counterclockwise, and is at ε^+ radians counterclockwise from the positive x (east-west) axis at time $t = 0$; while the latter has length a^-, rotates clockwise, and is at ε^- radians counterclockwise from the positive x axis at $t = 0$.

From linearity, the frequencies of the tidal current components are the same as the known frequencies of the motions of the sun and moon with respect to the earth. Thus the frequencies specified for all constituents have been calculated from the rates of change of the astronomical variables and the respective Doodson numbers. Though the program (Foreman 1978) is capable of including a maximum of 146 possible tidal constituents in the analysis, the inclusion of a particular tidal constituent in the analysis is made based on Rayleigh comparison constituent. For a record too short to resolve K_1 from P_1 or S_2 from K_2 (for example, the record at EAS), the P_1 and K_2 constituents were inferred from the amplitude ratios and phase differences determined from an adjacent mooring where P_1, K_1 and S_2, K_2 constituents were resolved. The numbers of tidal constituents thus included at western, central and eastern mooring are 60, 51 and 38 respectively. Once the tidal constituents are chosen, then the problem is to find the magnitude of the vectors

$$a^+ = \tfrac{1}{2}[(cx + sy)^2 + (cy - sx)^2]^{1/2} \tag{4a}$$

$$a^- = \tfrac{1}{2}[(cx - sy)^2 + (cy + sx)^2]^{1/2} \tag{4b}$$

and phases

$$\varepsilon^+ = \arctan[(cy - sx)/(cx + sy)] \tag{5a}$$

$$\varepsilon^- = \arctan[(cy + sx)/(cx - sy)], \tag{5b}$$

of equation (3) that best fit the series of observations $V(t_i)$, $i = 1, 2..N$. Here, cx, sx, cy and sy are the cosine and sine terms of x and y components of the series. To obtain optimum values of the magnitudes and phases of the vectors, a least square fit was employed. Finally, the phase of each constituent was represented as the Greenwich phase. This is defined as the difference between the astronomical argument for Greenwich and the phase of the observed constituent signal. The time-series was thus referred to GMT before subjecting to analysis.

3. Tidal ellipses

The M_2, S_2 and K_1 tidal ellipses thus computed are shown in figure 3. The parameters (semi-major axis, semi-minor axis, inclination and the Greenwich phase for P_1, K_1, M_2, S_2 and K_2) that define the ellipses are given in table 2. Table 3 provides the cosine and sine terms that were used to construct the ellipses, and their estimated standard deviations. To estimate the error limits for the ellipses, the following procedure based on Monte Carlo simulation was followed. Using the cosine (*cx*, *cy*) and sine (*sx*, *sy*) terms and their standard deviations (*cxerr*, *cyerr*, *sxerr*, *syerr*), 10000 ellipses were generated by redefining the cosine and sine terms as *cxu*, *cyu*, *sxu* and *syu* by the relationship

$$cxu = cx - cxerr + 2 \times r1 \times cxerr, \tag{6a}$$

$$sxu = sx - sxerr + 2 \times r2 \times sxerr, \tag{6b}$$

etc.. where $r1$, $r2$, $r3$ and $r4$ are numbers distributed between 0 and 1 generated by a pseudo-random number generator. The envelope of these ellipses are considered as the error limits for the ellipses shown in figure 3. The M_2 ellipses along with their error limits (dotted ellipses) computed from the errors in cosine and sine terms are shown in figure 4. From this figure it is seen that the upper and lower ellipses are

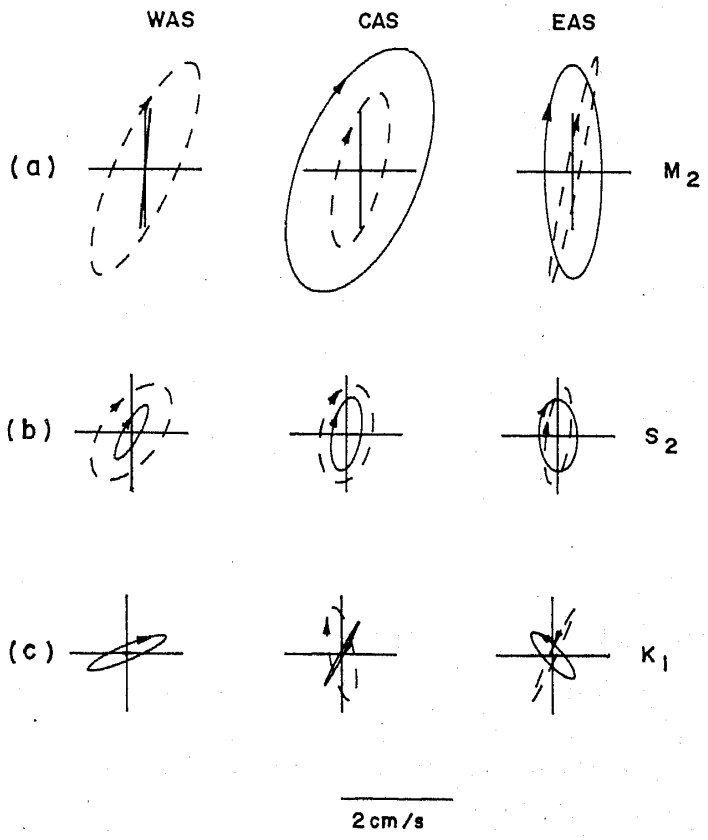

Figure 3. Semi-diurnal and diurnal tidal current ellipses, at three mooring locations (figure 2), obtained from the tidal analysis. (**a**) M_2, (**b**) S_2 and (**c**) K_1. The dashed curves represents the ellipses at lower current meters (please see table 1 for current meter depths).

Table 2. P_1, K_1, M_2, S_2, and K_2 tidal ellipse parameters. A negative sign for the minor axis indicates the clockwise rotation of the tidal current.

Location	Depth (m)	Tide	Semimajor (cm/s)	Semiminor (cm/s)	Inclination (deg)	Phase (deg)
WAS	1016	P_1	0·42	−0·20	14·0	336·1
		K_1	0·75	−0·13	22·6	8·9
		M_2	1·03	−0·01	85·1	42·6
		S_2	0·55	−0·14	59·8	117·2
		K_2	0·14	−0·07	25·3	78·7
	3016	P_1	0·16	−0·08	84·9	195·8
		K_1	0·06	+0·02	5·8	336·7
		M_2	2·01	−0·53	65·2	66·0
		S_2	0·99	−0·51	52·3	132·6
		K_2	0·26	−0·08	53·0	135·2
CAS	706	P_1	0·27	+0·13	78·1	101·7
		K_1	0·63	+0·03	60·0	56·5
		M_2	2·24	−1·08	66·7	93·6
		S_2	0·65	−0·26	79·7	122·2
		K_2	0·08	−0·05	152·9	91·2
	2906	P_1	0·13	−0·03	71·0	28·3
		K_1	0·82	−0·23	101·4	77·3
		M_2	1·38	−0·41	75·1	58·6
		S_2	0·86	−0·47	77·7	164·5
		K_2	0·25	−0·05	66·8	110·3
EAS	1379	P_1	0·31	+0·12	152·4	299·3
		K_1	0·54	+0·15	134·4	257·8
		M_2	1·84	−0·51	90·6	76·0
		S_2	0·62	−0·35	93·0	93·8
		K_2	0·05	−0·01	166·3	55·2
	2779	P_1	0·15	−0·01	33·6	222·7
		K_1	0·89	+0·06	64·0	270·6
		M_2	2·02	−0·12	78·3	132·7
		S_2	0·84	−0·21	81·7	189·7
		K_2	0·33	−0·19	78·3	173·2

distinct and the variations represented by each of them are significant. The error limits constructed for the ellipses of other constituents also were similar.

The M_2 tidal ellipses (figure 3) at all the 6 current meters show two important features. First, inclination of the major axis is more or less the same ($75 \pm 10°$) in all the six records. Second, the magnitude of the major axis is also about the same at the upper and the lower levels. We interpret these features to imply that barotropic motion forms a significant component of M_2 constituent. If the motion was entirely due to barotropic tides, the ellipses would be the same at different depths in the region expected to be free from the influence of friction. The variations in the ellipses over the water column are an indication that baroclinic motion also contributes. The ellipse at the upper current meter on the western mooring is rectilinear (with a larger major axis compared to the minor axis) compared to the deeper one. At the eastern mooring the deeper ellipse is more rectilinear than the upper ellipse. The S_2 currents also show a consistent pattern in their orientation and magnitude of the major axis

Table 3. Cosine and sine terms of M_2, S_2 and K_1 tidal current vectors.

Location	Depth (m)	Tide	*cx* (*cxerr*)	*sx* (*sxerr*)	*cy* (*cyerr*)	*sy* (*syerr*)
WAS	1016	M_2	−0·077	−0·028	−0·881	−0·367
			(0·060)	(0·060)	(0·060)	(0·060)
		S_2	0·069	−0·283	−0·150	−0·436
			(0·060)	(0·060)	(0·060)	(0·060)
		K_1	−0·543	0·540	−0·106	0·328
			(0·060)	(0·060)	(0·060)	(0·060)
	3016	M_2	0·843	−0·337	0·897	−1·465
			(0·074)	(0·074)	(0·072)	(0·072)
		S_2	0·692	0·105	0·557	−0·589
			(0·074)	(0·074)	(0·072)	(0·072)
		K_1	−0·041	0·055	−0·017	−0·005
			(0·074)	(0·074)	(0·072)	(0·072)
CAS	706	M_2	0·754	−0·989	−0·756	−1·816
			(0·063)	(0·063)	(0·056)	(0·056)
		S_2	−0·057	−0·267	−0·613	−0·086
			(0·063)	(0·063)	(0·056)	(0·056)
		K_1	0·259	0·231	0·394	0·450
			(0·063)	(0·063)	(0·056)	(0·056)
	2906	M_2	0·017	−0·495	−0·965	−0·797
			(0·037)	(0·037)	(0·054)	(0·054)
		S_2	−0·202	−0·431	−0·808	0·143
			(0·037)	(0·037)	(0·054)	(0·054)
		K_1	−0·292	−0·073	0·287	0·836
			(0·037)	(0·037)	(0·054)	(0·054)
EAS	1379	M_2	0·431	−0·207	−0·798	−1·526
			(0·049)	(0·049)	(0·065)	(0·065)
		S_2	−0·001	−0·317	−0·594	0·019
			(0·049)	(0·049)	(0·065)	(0·065)
		K_1	−0·326	0·349	0·049	−0·480
			(0·049)	(0·049)	(0·065)	(0·065)
	2779	M_2	−0·396	−0·015	−1·793	0·450
			(0·042)	(0·042)	(0·046)	(0·046)
		S_2	−0·114	0·093	0·161	0·655
			(0·042)	(0·042)	(0·046)	(0·046)
		K_1	0·443	0·170	0·781	0·456
			(0·042)	(0·042)	(0·046)	(0·046)

(figure 3). The orientations appear to remain stable at both upper and lower current meters at the western, central and eastern moorings. The consistency in the ellipses suggests barotropic tidal activity. The magnitude of S_2 (semi-major axis 1·0 cm/s) currents are smaller than M_2 (about 2·2 cm/s). Thus the S_2 signal-to-noise ratio is poorer.

The K_1 (semi-major axis 0·89 cm/s) currents do not show a consistent pattern and are smaller than M_2 (about 2·2 cm/s). The K_1 ellipse from the bottom current meter at western mooring is practically non-existent. Clockwise and anti clockwise rotations are present in the ellipses. From the complexity of the ellipses it would appear that the K_1 tidal currents of the deep mid-Arabian sea do not have a measurable barotropic

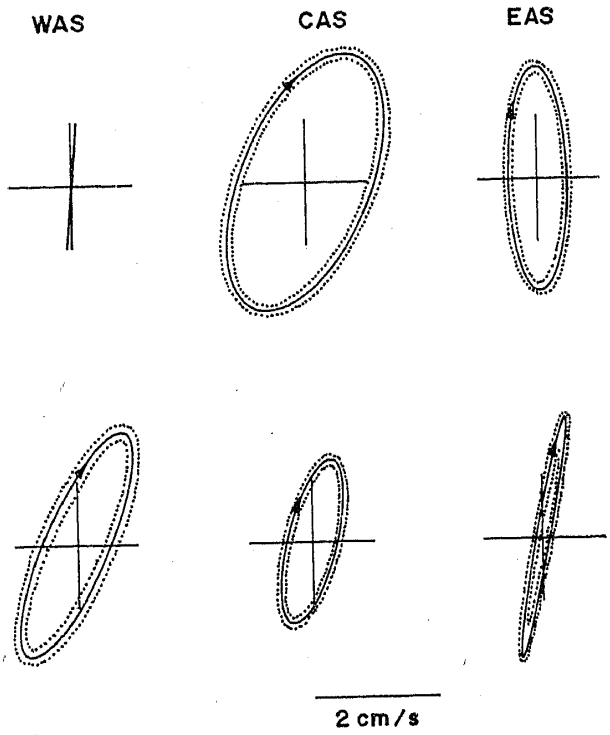

Figure 4. M_2, tidal ellipses at three locations (WAS, CAS and EAS) and their error limits (dotted ellipses).

component. Similar is the case of P_1 (semi-major axis 0·42 cm/s) and K_2 (semi-major axis 0·33 cm/s) ellipses. The P_1 ellipses also show both clockwise and anti-clockwise rotations.

4. Barotropic tidal ellipses

Had the density in the region of observation been uniform, the tidal currents would have been barotropic, with the tidal ellipses at both upper and lower level being the same, and the motion would then be the result of propagation of surface gravity waves alone. Well-defined vertical stratification, however, is observed in the Arabian Sea and this is expected to support the propagation of internal waves. The result is that the tidal ellipses described above are influenced by both barotropic mode (surface gravity waves) and baroclinic mode (internal waves). To get an idea of the relative contributions of the barotropic mode we adopted a simple procedure based on the assumption that the average of the upper and the lower currents will represent the barotropic currents, and the deviation from this average will represent the baroclinic currents at the two levels. However, it may be noticed that the above assumption must be viewed with caution when the number of current meters available in the water column is only two. To compute the barotropic (mean) tidal currents first we have re-computed the hourly tidal currents at each level (north-south) and east-west components) from the respective tidal ellipses (figure 3, table 2) following Foreman (1978). Then these hourly current components from the upper and lower current meters were averaged to obtain the barotropic contribution. The barotropic ellipses

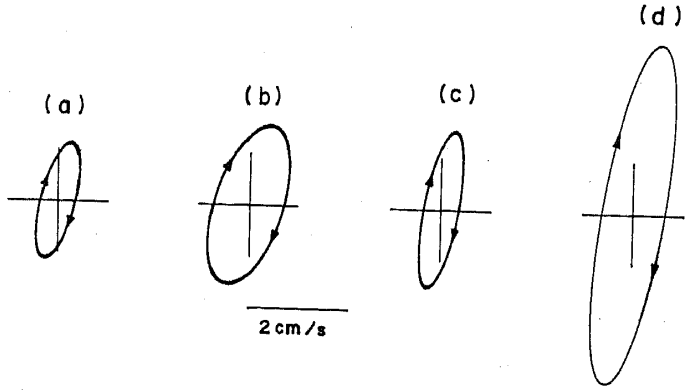

Figure 5. The barotropic M_2 tidal current ellipses obtained at (**a**) western, (**b**) central and (**c**) eastern mooring. (**d**) M_2 tidal current ellipse reproduced from Pekeris and Accad (1969).

computed for M_2 tidal currents are shown in figure 5. As an accuracy check, the M_2 ellipses may be compared with those predicted by numerical solutions to the Laplace tidal equations (Pekeris and Accad 1969). An ellipse shown in Pekeris and Accad's figure 12 lies close to the eastern mooring (15°32′N 68°44′E) and is also reproduced in figure 5 for comparison. The orientation of the predicted ellipse is virtually identical to the computed ellipse at the eastern mooring. However, the modelled amplitude is larger. Also, it may be noted that the modelled amplitude is well beyond the error limits (figure 4) given for the computed amplitudes. A similar situation prevailed in the Bay of Biscay (Gould and Mckee 1973). It is likely that the difference in amplitudes is a consequence of the magnitude of friction coefficient used in the model. The fact that the orientations of the predicted and the computed ellipses match encourages us to believe that the coefficients in the model could be tuned to improve agreement with observations. We also note our reservations about the method adopted to compute the barotropic ellipse from the limited number of current meters. Within the constraints due to this reservation, the results suggest the following. Barotropic tidal currents in the deep mid-Arabian sea are elliptical but relatively weak, with the amplitude of the semi-major axis of the largest component (M_2) being only 1·63 cm/s at the central and 1·56 cm/s at the eastern mooring. At the western mooring the magnitude of semi-major axis is the lowest, about 1·18 cm/s.

5. Baroclinic tides and internal waves

Baroclinic tides are believed to be generated by interaction of barotropic tides with bottom topography and/or the density stratified water column, and, modified by the influence of the earth's rotation. In a flat bottom ocean, horizontally propagating baroclinic motion at a frequency, ω, can be expanded as the sum of a series of vertical modes. The modes associated with the buoyancy frequency profile can be calculated by solving the vertical structure equation for the vertical velocity W (Roberts 1975):

$$(\omega^2 - f^2)\frac{\partial}{\partial z}\left(\bar{\rho}\frac{\partial W}{\partial z}\right) - \bar{\rho}(\omega^2 - N^2)k^2 W = 0, \tag{7}$$

where $\bar{\rho}$ is the mean density, $N^2 = -(g/\rho)(\partial\bar{\rho}/\partial z)$ is the square of the Brunt Vaisala

frequency, k^2 the eigenvalue (the square of the horizontal wave number), f the Coriolis parameter and ω the frequency of the wave. Theoretically, one can obtain the baroclinic tidal ellipses for each of these modes by projecting the tidal ellipses given in figure 3 onto the first few baroclinic (internal) modes by a least square fit (Magaard and McKee 1973). However, we cannot follow this procedure due to lack of sufficient number of current meters over the water column. Nevertheless, we have computed the first few baroclinic modes to obtain the horizontal length scales of baroclinic tidal motions in the Arabian Sea. To compute the modes the buoyancy frequency profile (figure 6) associated with the annual mean density profiles were calculated using the Levitus (1982) data available closest to the mooring sites (16°30′N, 60°32′E; 14°30′N, 64°30′E and 15°30′N, 68°30′E). Equation (7) was solved subject to the boundary conditions $W = 0$ at surface and bottom. A NAG fortran library routine (subroutine DO2kef) available to solve the Sturm-Liouville equation was used to obtain the eigenvalue k^2 and eigenfunction W. As the horizontal velocities were proportional to the z derivative of the vertical velocity, the eigenfunctions were differentiated to obtain the eigenfunctions for horizontal velocity components. The results for the four internal modes are shown in figure 6 and the corresponding wavelengths for these modes are given in table 4. The table suggests that no wavelengths

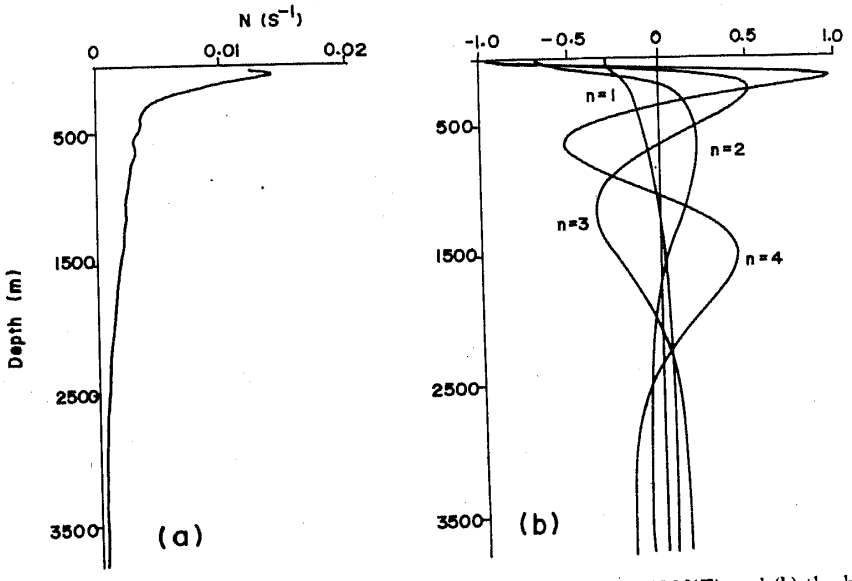

Figure 6. (a) The buoyancy frequency profile (at 15°30′N, 68°30′E) and (b) the horizontal velocity component eigenfunctions for the first four baroclinic modes at eastern mooring (EAS).

Table 4. Wavelengths (in km) of the baroclinic modes at Western, Central and Eastern moorings.

Mode no.	WAS	CAS	EAS
1	117·98	118·71	115·49
2	65·33	68·03	67·02
3	42·58	43·10	42·89
4	30·87	31·33	30·95

are greater than 120 km. This horizontal scale of motion is well below 500 km, the distance separating the current meter moorings. We, therefore, conclude that even if baroclinic motions influence tidal motion, they are unlikely to be correlated at any two adjacent moorings.

6. Concluding comments

Though the moorings which provided the data used in this study were not designed with tidal studies in mind, the data have been useful to define some of the features of the tidal motion in the mid-Arabian Sea. The magnitudes of M_2 barotropic tide (1·2–1·6 cm/s) are similar to those observed in the mid-Atlantic, 1·0 cm/s (Magaard and McKee 1973) and mid-Pacific, 1·8 cm/s (Weisberg *et al* 1987). The overall features that have been identified here through the construction of tidal ellipses for the M_2, S_2 and K_1 tidal constituents are consistent with the patterns of tidal propagation shown in figure 1. The M_2 amplitudes computed here and the amplitudes of M_2 elevations shown in figure 1 are almost double those for S_2 and K_1. The tidal ellipses given in the last three sections appear to be the first such estimates based on direct current observations. They should therefore be of interest in attempts at modelling the tidal currents in the region.

Acknowledgements

We thank D Sundar and R R Nair (National Institute of Oceanography, Goa) and V Ittekkot (University of Hamburg, Hamburg) for their help in the deployment and retrieval of the moorings. The mooring programme was jointly supported by the Council of Scientific and Industrial Research, New Delhi, and the Federal German Ministry for Research and Technology, Bonn. We thank Prof. Theodore Foster of the University of California for useful comments on an earlier version of this paper and for his advice on improving the quality of our analysis. Critical comments from four anonymous reviewers are also acknowledged gratefully.

References

Cartwright D E and Ray R D 1990 Oceanic tides from GEOSAT altimetry; *J. Geophys. Res.* **95** 3069–3090

Foreman M G G 1977 Manual for tidal heights analysis and prediction. Institute of Ocean Sciences (Canada); Pacific Marine Science Report, 77–10, 97 pp

Foreman M G G 1978 Manual for tidal current analysis and prediction. Institute of Ocean Sciences (Canada); Pacific Marine Science Report, 78–6, 70 pp

Godin G 1972 *The analysis of tides* (Toronto: University of Toronto Press) 264 pp

Gould W J and McKee W D 1973 Vertical structure of semi-diurnal tidal currents in the Bay of Biscay; *Nature (London)* **244** 88–91

Levitus S 1982 Climatological Atlas of the World Ocean; NOAA Professional paper 13, US Department of Commerce, Washington, DC

Magaard L and McKee W D 1973 Semi diurnal tidal currents at site 'D'; *Deep Sea Res.* **20** 997–1009

Nair R R, Ittekkot V, Mainginini S J, Ramaswamy V, Haake B, Degens E T, Desai B N and Honjo S 1989 Increased particle flux to the deep ocean related to monsoons; *Nature (London)* **338** 749–751

Pekeris C L and Accad Y 1969 Solution of Laplace's equations for the M_2 tide in the world oceans; *Phil. Trans. R. Soc. (London)* **A265** 413–436

Regal R and Wunsch C 1973 M_2 tidal currents in the western north Atlantic; *Deep Sea Res.* **20** 493–502

Roberts J 1975 *Internal gravity waves in the ocean* (New York: Marcel Dekker) 274 pp

Schwiderski E W 1979 Global Ocean tides part II: The semi-diurnal principal lunar tide (M_2), atlas of tidal charts and maps; Naval Surface Weapons Center Technical report No. 79–414

Schwiderski E W 1980 Ocean tides II: A hydrodynamic interpolation model; *Mar. Geod.* **3** 219–255

Schwiderski E W 1981a Global Ocean tides part III: The semi-diurnal principal solar tide (S_2), atlas of tidal charts and maps; Naval Surface Weapons Center Technical report No. 81–122

Schwiderski E W 1981b Global Ocean tides part IV: The diurnal luni-solar declination tide (K_1), atlas of tidal charts and maps; Naval Surface Weapons Center Technical report No. 81–142

Shetye S R, Shenoi S S C and Sundar D 1991 Observed low frequency currents in the deep mid Arabian sea; *Deep Sea Res.* **38** 57–65

Weisberg R H, Halpern D, Tang T Y and Hwang S M 1987 M_2 tidal currents in the eastern equatorial Pacific ocean; *J. Geophys. Res.* **15** 3821–3826